

Fabrication of Heterostructure InN/photo-electrochemical Etched Silicon (110)

M. Amirhoseiny*, Z. Hassan, S. S. Ng

Nano-Optoelectronics Research and Technology Laboratory, School of Physics, Universiti Sains Malaysia, 11800 Penang, Malaysia

*E-mail: Amirhoseiny_m@yahoo.com

Received: 22 December 2012 / *Accepted:* 24 February 2013 / *Published:* 1 April 2013

We report on the structural and optical characteristics of heterostructure InN/PSi/n-type Si(110) grown by radio frequency (RF) sputtering at room temperature. Photo-electrochemical etched Si (PSi) layers were synthesized on n-type silicon (110) wafer. PSi is used as an intermediate layer between silicon and InN and it presents a groove structure based on SEM results. The blue shift in the PL and Raman peaks after etching is consequent of the quantum confinement effect and defect states of surface Si nanocrystallites complexes and hydrogen atoms of the Photo electrochemical etched Si (110) samples. X-ray diffraction measurement confirms that the deposited InN film has (101) preferred growth orientation and wurtzite structure. Two Raman and infrared active modes of $A_1(\text{LO})$ and $E_1(\text{TO})$ of the wurtzite InN are obviously observed. These results leading to conclude that the wurtzite InN thin film with (101) preferred growth orientation was successfully grown on Photo-electrochemical etched Si.

Keywords: Electrochemical etching, InN, Silicon (110), heterostructure

1. INTRODUCTION

Indium nitride (InN) has a wurtzite crystal structure with a band gap ranging from 0.7 eV to 1.9 eV [1]. InN is an interesting semiconductor material because of its potential applications in optoelectronic devices, such as high efficiency solar cells, high electron mobility sensors, and transistors [2-5]. However, InN has received little attention compare to GaN and AlN mostly due to the inherent difficulty of its preparation in stoichiometric form [6]. In addition, high-grade single crystal InN is difficult to grow due to its low dissociation temperature [5] and less suitable substrates. Because of the low dissociation temperature, InN film should be deposited at a low temperature to avoid re-evaporation of N atoms. Consequently, reactive sputtering is one of the most promising techniques from the viewpoint of low temperature film growth. Previously the synthesizing of InN layers on

sapphire and glass substrates using reactive sputtering has been reported [7, 8]; while a few works on deposition of the InN thin films on different orientations of Si substrate have been recently investigated [9-11]. Electrochemical wet etching of Si under controlled conditions creates the formation of nanocrystalline Si where quantum confinement of photoexcited carriers proceeds to an increased radiative transition rate and a band gap opening[12]. Etched Si layers electrochemically formed on p-type Si (110) wafers reveal strong in-plane birefringence [13]. Birefringent etched Si layers demonstrate properties of a uniaxial negative crystal whose optical axis lies along the [001] in-plane crystallographic direction[12, 14]. However, the disordered distribution of nanocrystal sizes and surface compositions restrict a real engineering of etched Si properties. It is well known that for producing a good device, several factors must be taken into account.

In the current study, heterostructure of n-type InN/PSi/Si(100) were successfully fabricated by radio frequency (RF) sputtering at room temperature. The structure and optical properties of the InN heterostructure by Photoelectrochemical etched of (110) oriented Si inner layer were investigated. To the best of our knowledge, this has never been reported so far.

2. EXPERIMENTAL

Photo-electrochemical etched Si layers were prepared on n-type (110) oriented Si wafer with 0.002-0.005 $\Omega\cdot\text{cm}$ resistivity. The etching process took place in a Teflon cell with aluminium base plat. The Si (110) sample was subsequently dipped into a mixed solution of HF: C₂H₅OH (1:4 in volume) under a 60W lamp illumination at a constant current density of 20 mA/cm² for 25 minute. The porosity processing condition have been optimized before [12, 15]. Ethanol is used as a surface active agent and also for removing the bubbles of hydrogen created during etching. Typical wet etching set-up is schematically shown in Figure 1. In order to prepare etched Si under uniform current density, the anodization process was done at room temperature (around 25°C). After etching, the etched Si samples were rinsed in ethanol and dried in nitrogen shower.

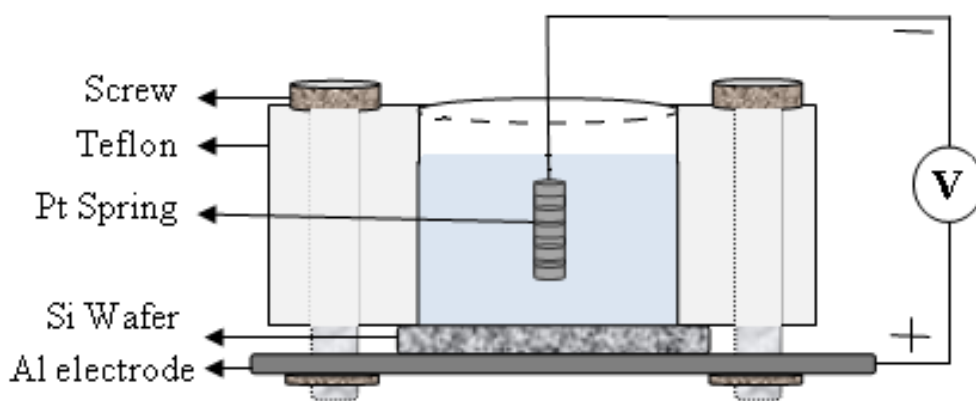


Figure 1. Schematic of wet etching set up.

Epitaxial films of InN approximately 0.7 μm thick were grown on Photo-electrochemical etched Si (110) layer by reactive RF sputtering of a pure indium (In) target (99.99%), in an argon (Ar) and nitrogen (N_2) atmosphere at room temperature. The base pressure was around 2×10^{-5} mbar, and the deposition was maintained at a constant pressure of approximately 8×10^{-3} mbar. The applied RF power was 50 W, and the reactive gas concentrations of Ar: N_2 was 14:6 sccm. The obtained films were characterized with X-ray diffraction (XRD, PANalytical X'pert PRO MRD PW3040), atomic force microscopy (AFM, Bruker Dimension Edge), scanning electron microscopy (SEM, FESEM Nova NanoSEM 450) and energy dispersive X-ray spectroscopy (EDX). The optical properties of InN layers were examined by Fourier transform infrared (FTIR, Perkin Elmer Spectrum GX) and micro-photoluminescence and Raman spectroscopy (Jobin Yvon HR 800 UV) at room temperature.

3. RESULTS AND DISCUSSION

Figure 2(a) presents the SEM image of the Photo electrochemical etched Si layer formed on the n-type c-Si (110) sample. The surface of the c-Si sample was completely etched but the SEM observations discover the different morphology of the photo-electrochemical etched Si (110) surfaces as compared to other Si orientations. The pore formation progress is correlated to the crystalline structure of the Si wafers [16]; For (110) orientation of Si, we observed the groove instead of the formation of pore. The schematic arrangement of (110) orientation of Si atoms is illustrated in Fig. 2 (b) [17]. The zigzag arrays of Si atoms along $[1\bar{1}0]$ and channels between the arrays are visible. Si (110) wafers have three equivalent $\langle 100 \rangle$ axes: $[001]$ lies in the plane of the layer while another two $[100]$ and $[010]$ are tilted at 45° to the (110) surface.

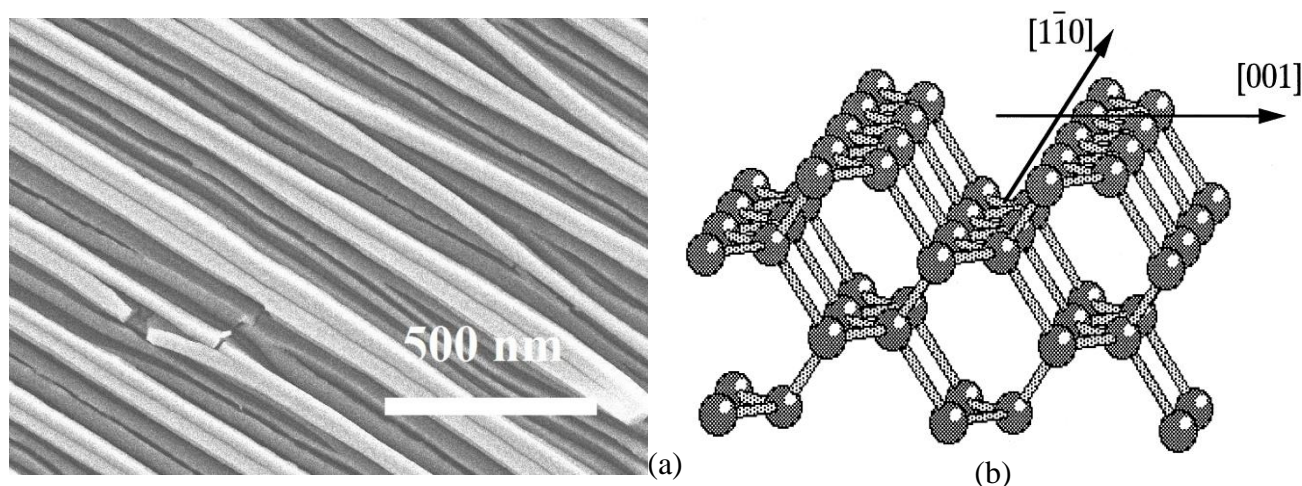


Figure 2. SEM images of (a) Porous Si(110), and (b) Schematic of the atomic arrangement of Si (110) plane [17].

The projection of these two axes to the surface plane of the layer coincides with the $[110]$ crystallographic direction. These three axes are not in-plane equivalent and (110) etched Si layers

become highly optically anisotropic [18]. Since groove formation usually follows the $\langle 100 \rangle$ axes of Si wafer [16, 19] and based on Fig.2(b), the morphology of photo-electrochemical etched Si (110) shows grooves in (100) direction. Note that although high magnification measurements were performed, no significant pores can be observed and this may most probably due to the pores size is too fine (roughly $< 10\text{nm}$).

The morphology and nanocrystalline structure of the InN thin films deposited on etched Si (110) were also examined by scanning electron microscopy (SEM). Figure 3 (a) shows that the film consists of agglomerated nanocrystals. The form of nano particles is an effect of lattice mismatched materials where the nucleation of the nitride films is initiated on protruding crystals on the rough underlying substrate. The EDX results for the InN thin films grown on PSi (110) substrate are summarized in Fig. 3 (b). The graph shows that InN sample grown in a good stoichiometric form. Oxygen is viewed as a common contaminant of InN in samples. Oxygen is present at the interface of the substrates, which probably arises from SiO_2 during the etching, In_2O_3 , or oxygen substitution on nitrogen sites [20]. Despite the contamination by oxygen in the formation of In_2O_3 or SiO_2 , no peak corresponding to the presence of these phases is observed in the X-ray patterns.

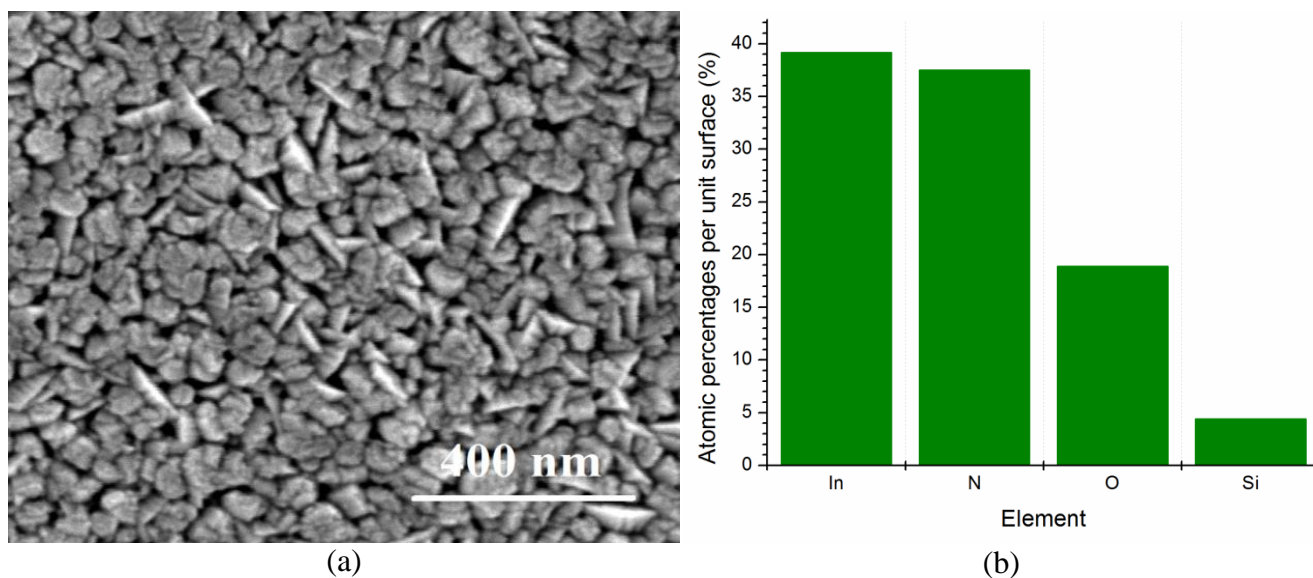


Figure 3. (a). SEM images and (b) EDX results of InN thin films grown on PSi (110) layer.

Figure 4 shows the XRD results of InN films deposited on PSi(110) substrate, the XRD spectrum of photoelectrochemical etched Si(110) is shown in the inset. The exhibited pattern was indexed by using the hexagonal crystal system (JSDC code, 01-079-2498). The XRD results revealed diffraction peaks corresponding to (101), (002) and (100) plans related to the hexagonal structure of InN. Subsequently, this leads us to conclude that the deposited InN thin film has wurtzite structure with preferred orientations of InN (101). In order to access the InN crystalline quality, crystalline size, lattice constant, and lattice mismatch, the strongest InN(101) reflection peak is analyzed in detail and the results summerized in Table. 1.

Table 1. Full-width at half maximum (FWHM) of InN (101) diffraction peak, crystallite size, Lattice constant, and the mismatch between InN and different substrates.

	Crystallite size [nm]	2θ[°]	FWHM [°]	Lattice Constant of InN <i>c</i> (Å)	Mismatch between InN and substrates
InN/PSi(110)	24.1	33.04	0.394	5.74	0.05

The average InN crystalline size (*D*) can be calculated using the Scherrer formula [21],

$$D = \frac{0.89\lambda}{B \cos \theta_B}, \tag{1}$$

where *B* is the full width at half maximum of the InN (101) diffraction peak, λ is the wavelength of the X-ray (1.5406 Å), and θ_B is the Bragg diffraction angle of InN(101). The XRD result indicates that the layer consists of InN nanocrystals with mean crystalline size of 24.1 nm. The crystal size may depend on the interface formation and defect structures, which may also arise from the lattice mismatch, substrate surface energy and the difference of crystalline structure between the substrates and deposited films.

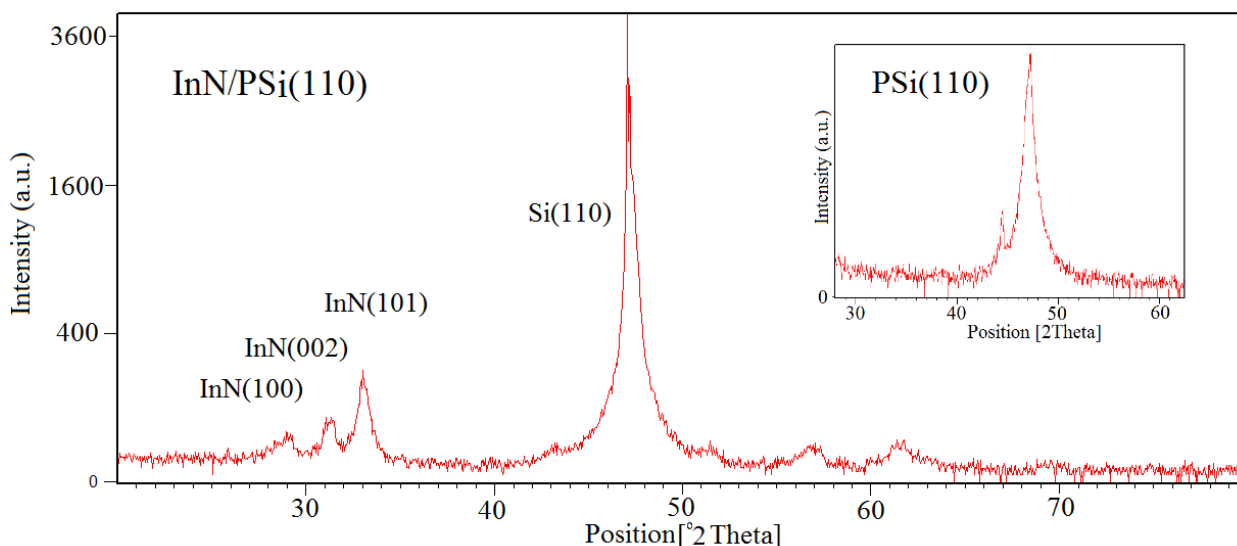


Figure 4. XRD spectrum of InN thin film grown on Psi(110) layer, the XRD spectrum of photoelectrochemical etched Si(110) is shown in the inset.

The lattice mismatch between the InN thin film and the porous Si(110) layer is calculated by comparing the (101) planes of InN and PSi(100) using the following relation [22]:

$$\epsilon_{zz} = \frac{c' - c}{c}, \tag{2}$$

where c' represents the lattice constant of the InN thin film estimated from XRD data and c is the lattice constant of PSi layer. For the hexagonal structure, the values of the lattice constants a and c , which indicate the strain present in the sample are calculated according to the XRD value, the distance between adjacent planes in the set of planes and Miller-Bravais indices (hkl) [23]. The obtained lattice mismatch for InN thin film grown on the PSi layer were 0.05 along the c axis. The positive value of mismatch revealed the tensile strain for InN thin films.

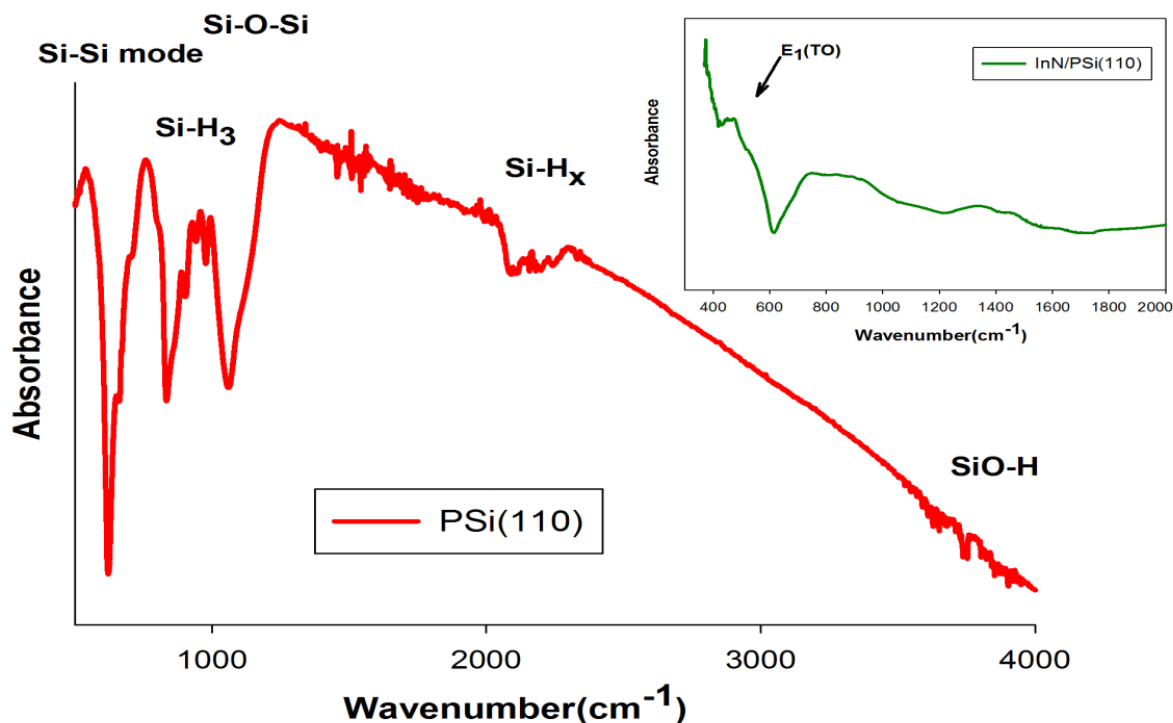


Figure 5. FTIR absorption spectra of photo-electrochemical etched Si (110) sample and InN thin films grown on PSi layer.

The FTIR reflectance spectrum of PSi (100) and InN on PSi layer as measured at an incident angle of 16° are shown in Figure 5. For PSi layer, the absorption dips at around 950 cm^{-1} , 2089 cm^{-1} and 2119 cm^{-1} are associated to Si-H_x bond vibration modes. The 1150 cm^{-1} peak is due to the Si-O-Si stretching mode which indicates that the PSi layer is already partially oxidized. The peak at 616 cm^{-1} presented the binding states of Si-Si vibration mode in bulk Si. The appearance of the Si-H_x vibrational bands is consistent with the expected porous Si properties[16]. The InN spectrum shows a prominent peak centered at 486 cm^{-1} . This feature is corresponding to the E₁(TO) phonon mode of the InN. Since the spectral strength of A₁(LO) phonon mode of InN is weak in nature as compared to E₁(TO) mode, it cannot be clear seen in FTIR reflectance spectrum. Nevertheless, the mode due to the A₁(LO) is obvious in Raman spectrum.

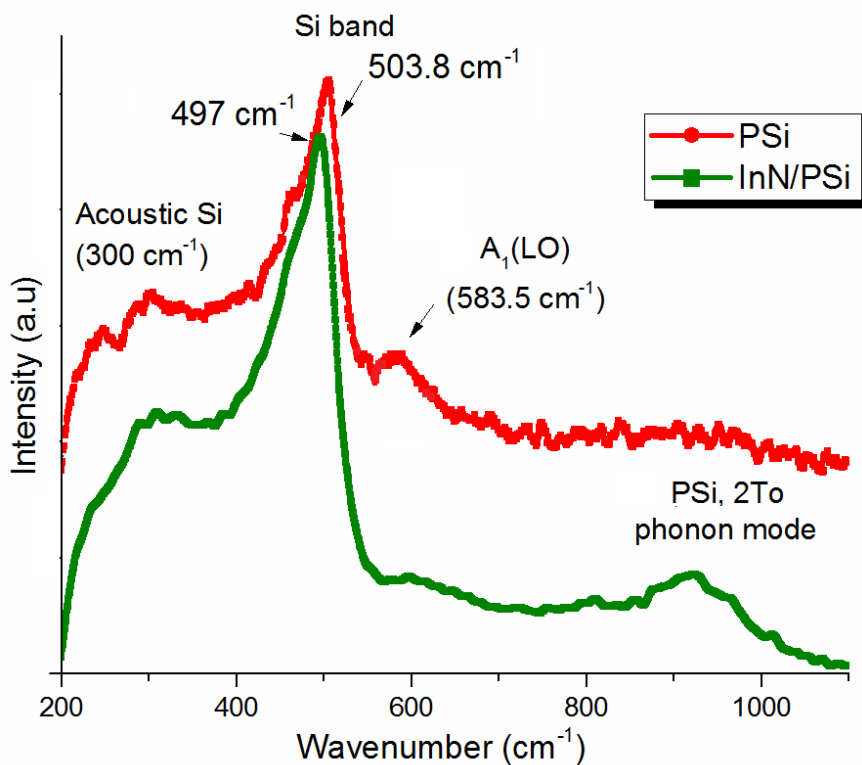


Figure 6. Raman spectra of photo-electrochemical etched Si (100) sample and InN thin film grown on PSi layer.

Figure 6 shows Raman spectra for porous Si (110) sample and InN thin film grown on PSi layer. The Raman peak of bulk crystalline Silicon (c-Si) is at 519 cm^{-1} [9]. After porosification, the Raman peak position significantly shifted to toward lower frequency due to the nanostructure effects. Raman spectra also show an extra peak at around 940 cm^{-1} . This additional peak is induced by transverse-optical (2TO) phonon overtones [24]. This mode is due to the disorder present in photo-electrochemical etched Si around the pores during their formation. During etching, the dissolution process results in a layer of disordered amorphous Si immediately around the pores[12]. The Raman scattering experiment was performed in the z (x, unpolarized) z scattering configuration, where the z and z are the directions of incident and scattered light.

Under this configuration, the allowed zone-center phonon modes of wurtzite InN are E_2 (Low), E_2 (High), and A_1 (LO). For InN thin films, A relatively fairly broad feature corresponding to the A_1 (LO) mode of InN is observed at 583.5 cm^{-1} . Besides that, it is found that the obtained A_1 (LO) is about 4 cm^{-1} lower than that of the strain-free bulk InN (586 cm^{-1}). This is most likely due to the compressive stress in the InN thin film (as discussed previously) as well as the free carrier coupling effects [25]. Another allowed Raman mode of E_2 (high) that is located at 488 cm^{-1} , is hardly detected because it has been covered by the stronger Si peak.

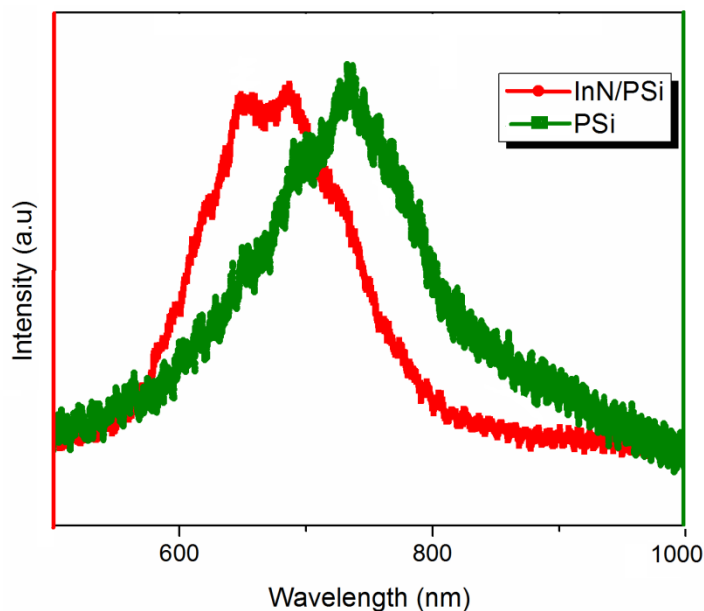


Figure 7. PL spectra of photo-electrochemical etched Si (110) sample and InN thin film grown on PSi layer.

Figure 7 shows the PL spectra of porous Si (110) sample and InN film grown on PSi layer at room temperature. PSi and InN samples showed a broad peak situated around 660 nm and 736 nm, respectively. The PL effect of PSi sample is associated to the quantum confinement effects based on nanoscale crystalline structures and also the formation of new chemical bonding on the etched Si surface [26, 27]. The observed PL peak energy is the sum of the band energy and the energies of sub-bands in which optical transitions take place. For InN sample, the energy emission peak (1.68 eV), which is produced by electron transitions from the conduction band to the valence band, is very close to the optical gap energy of polycrystalline InN, as previously reported [1]. The difference between the band gaps of 1.68 eV, which is obtained in this work, and 0.7 eV, which is attributed to pure materials, can be attributed to different effects. The band gap may increase with increasing carrier concentration, also referred to as the Moss–Burstein shift [28]. This effect occurs when the carrier concentration exceeds the conduction band edge density of states and the Fermi level is positioned within the conduction band. Thus, the Moss–Burstein shift leads to a higher InN band gap. In addition, the presence of oxygen has been suggested to bring out higher band gaps, as observed in some InN-based materials [29].

4. CONCLUSIONS

InN/PSi/n-Si heterostructure was successfully fabricated by reactive RF magnetron sputtering technique at low temperature. InN based heterostructures can be used as a IR detector . photo-electrochemical etching of n-type silicon (110) with grooving structure was used as a inner layer in InN based hetrostructure. The etched Si (110) samples revealed a PL peak in the visible spectral range which can be attributed to the crystal size, defect state and also the formation of new chemical bonding

on the etched Si surface. Poly-crystalline wurtzite structure of InN is verified by the X-ray diffraction with preferred orientations of InN(101). The blueshift of the Raman $A_1(\text{LO})$ mode implies a compressive stress on the InN film due to the lattice mismatch between the InN film and Porous Si layer. A strong PL peak was observed for InN case in the energy range 1.68 eV at room temperature. We believe that Moss–Burstein shifts led to a higher InN band gap in this work.

ACKNOWLEDGMENT

Financial support from ERGS, PRGS grant No. 1001/PFIZIK/844071 and University Sains Malaysia are gratefully acknowledged.

References

1. K. Butcher, T. Tansley, *Superlattices Microstruct.*, 38 (2005) 1-37.
2. H. Nguyen, Y. Chang, I. Shih, Z. Mi, Selected Topics in Quantum Electronics, *IEEE Journal of*, (2011) 1-8.
3. W.-J. Lai, S.-S. Li, C.-C. Lin, C.-C. Kuo, C.-W. Chen, K.-H. Chen, L.-C. Chen, *Scr. Mater.*, 63 (2010) 653-656.
4. N. Miller, J. Ager, H. Smith, M. Mayer, K. Yu, E. Haller, W. Walukiewicz, W. Schaff, C. Gallinat, G. Koblmuller, *J. Appl. Phys.*, 107 (2010) 113712-113718.
5. M. Amirhoseiny, Z. Hassan, s.s. Ng, I. Chuah, M.A. Ahmad, Y. Yusof, *Int. J. Mod Phys B*, 26 (2012) 1250137-1250139.
6. Motlan, E.M. Goldys, T.L. Tansley, *J. Cryst. Growth*, 241 (2002) 165-170.
7. M. da Silva, D. David, I. Pepe, A. Ferreira da Silva, J. de Almeida, A. Gazoto, A. dos Santos, L. Cardoso, E. Meneses, D. Graybill, *Thin Solid Films*, 520 (2012) 4848–4852.
8. O. Takai, K. Ikuta, Y. Inoue, *Thin Solid Films*, 318 (1998) 148-150.
9. M. Amirhoseiny, Z. Hassan, S.S. Ng, M.A. Ahmad, *Journal of Nanomaterials*, 2011 (2011) 579427.
10. X.-M. Cai, F. Ye, Y.-Q. Hao, D.-P. Zhang, Z.-H. Zhang, P. Fan, *J. Alloys Compd.*, 484 (2009) 677-681.
11. B.L. Zhang, G.S. Sun, Y. Guo, P.F. Zhang, R.Q. Zhang, H.B. Fan, X.L. Liu, S.Y. Yang, Q.S. Zhu, Z.G. Wang, *Appl. Phys. Lett.*, 93 (2008) 242107.
12. M. Amirhoseiny, Z. Hassan, N. Shashiong, *Elex*, 9 (2012) 752-757.
13. V.Y. Timoshenko, L.A. Osminkina, A.I. Efimova, L.A. Golovan, P.K. Kashkarov, D. Kovalev, N. Künzner, E. Gross, J. Diener, F. Koch, *Phys. Rev. B*, 67 (2003) 113405.
14. V.Y. Timoshenko, L. Osminkina, A. Efimova, M. Fomenko, L. Golovan, P. Kashkarov, D. Kovalev, N. Künzner, E. Gross, J. Diener, *Phys. Status Solidi C*, 2 (2005) 3461-3465.
15. M. Amirhoseiny, Z. Hassan, S.S. Ng, *Mod. Phys. Lett. B*, 26 (2012) 1250131-1250136.
16. M. Christophersen, J. Carstensen, S. Rönnebeck, C. Jäger, W. Jäger, H. Föll, *Journal of The Electrochemical Society*, 148 (2001) E267.
17. H. Miyata, K. Kuroda, *J. Am. Chem. Soc.*, 121 (1999) 7618-7624.
18. B. Goller, D. Kovalev, *Phys. Rev. B*, 83 (2011) 233303.
19. S.-Z.A. Lo, *Doctor of Philosophy thesis*, (2010).
20. B. Nag, *Phys. Status Solidi B*, 237 (2003) R1-R2.
21. J.I. Langford, A.J.C. Wilson, *J. Appl. Crystallogr.*, 11 (1978) 102-113.
22. M. Fitzpatrick, A. Fry, P. Holdway, F. Kandil, J. Shackleton, L. Suominen, in, National Physical Laboratory, 2005.
23. C. Suryanarayana, M.G. Norton, *X-ray diffraction: a practical approach*, Springer, 1998.

24. E. Edelberg, S. Bergh, R. Naone, M. Hall, E.S. Aydil, *J. Appl. Phys.*, 81 (1997) 2410.
25. Y. Peng, X. Xu, X. Hu, K. Jiang, S. Song, Y. Gao, H. Xu, *J. Appl. Phys.*, 107 (2010) 093519-093519-093515.
26. K. Behzad, W.M.M. Yunus, Z.A. Talib, A. Zakaria, A. Bahrami, *Int. J. Electrochem. Sci.*, 7 (2012) 8266-8275.
27. K.A. Salman, Z. Hassan, K. Omar, *Int. J. Electrochem. Sci.*, 7 (2012) 376-386.
28. P. Chakraborty, G. Datta, K. Ghatak, *Phys. B*, 339 (2003) 198-203.
29. V.Y. Davydov, A. Klochikhin, V.V. Emtsev, D. Kurdyukov, S. Ivanov, V. Vekshin, F. Bechstedt, J. Furthmuller, J. Aderhold, J. Graul, in, DTIC Document, 2002, pp. 68-71